


Article

Crystal Structure and Some Thermodynamic Properties of $\text{Ca}_7\text{MgSi}_4\text{O}_{16}$ -Bredigite

Xinjian Bao ^{1,2}, Mingyue He ³, Zhigang Zhang ⁴ and Xi Liu ^{1,2,*}

¹ Key Laboratory of Orogenic Belts and Crustal Evolution, Ministry of Education of China, Beijing 100871, China; xinjian.bao@pku.edu.cn

² School of Earth and Space Sciences, Peking University, Beijing 100871, China

³ School of Gemmology, China University of Geosciences (Beijing), Beijing 100083, China; Hemy@cugb.edu.cn

⁴ Key Laboratory of Earth and Planetary Physics, Institute of Geology and Geophysics, Chinese Academy of Sciences, Beijing 100029, China; zgzhang@mail.igcas.ac.cn

* Correspondence: xi.liu@pku.edu.cn

Abstract: Bredigite with the composition $\text{Ca}_7\text{MgSi}_4\text{O}_{16}$ ($\text{Ca}_7\text{MgSi}_4\text{O}_{16}$ -Bre) has been synthesized by a solid-state reaction method at 1.2 GPa and 1373 K for 7 days, and its structure has been determined by single-crystal X-ray diffraction data. Following a relevant genealogy analysis in the literature, we have refined the structure into two space groups, $Pnmm$ and $Pnn2$, and found that $\text{Ca}_7\text{MgSi}_4\text{O}_{16}$ -Bre belongs to the space group $Pnmm$, which can be essentially derived from the space group $Pnn2$ via an atomic coordinate transformation (with an average deviation of 0.039 Å only). Furthermore, some thermodynamic properties of the $\text{Ca}_7\text{MgSi}_4\text{O}_{16}$ -Bre have been obtained in this study. Using first-principles simulations based on density functional theory, the isothermal bulk modulus has been determined as 90.6(4) GPa with a pressure derivative of 5.7(1). Using density functional perturbation technique, the phonon dispersions and vibrational density of the states (VDoS) have been calculated. The VDoS has been combined with a quasi-harmonic approximation to compute the isobaric heat capacity (C_p) and standard vibrational entropy (S_{298}^0), yielding $C_p = 8.22(2) \times 10^2 - 3.76(6) \times 10^3 T^{-0.5} - 1.384(4) \times 10^7 T^{-2} + 1.61(8) \times 10^9 T^{-3} \text{ J mol}^{-1} \text{ K}^{-1}$ for the T range of 298–1000 K and $S_{298}^0 = 534.1(22) \text{ J mol}^{-1} \text{ K}^{-1}$.



Citation: Bao, X.; He, M.; Zhang, Z.; Liu, X. Crystal Structure and Some Thermodynamic Properties of $\text{Ca}_7\text{MgSi}_4\text{O}_{16}$ -Bredigite. *Crystals* **2021**, *11*, 14. <https://dx.doi.org/10.3390/cryst11010014>

Received: 29 November 2020

Accepted: 24 December 2020

Published: 26 December 2020

Publisher's Note: MDPI stays neutral with regard to jurisdictional claims in published maps and institutional affiliations.



Copyright: © 2020 by the authors. Licensee MDPI, Basel, Switzerland. This article is an open access article distributed under the terms and conditions of the Creative Commons Attribution (CC BY) license (<https://creativecommons.org/licenses/by/4.0/>).

Keywords: bredigite; single-crystal XRD; structure refinement; first-principle calculation; compressibility; heat capacity; standard vibrational entropy

1. Introduction

The continental crust of the Earth is rich in CaO and SiO_2 , and may form some special calcium silicates while it is subducted to certain depths of the mantle. Recently larnite-structured Ca_2SiO_4 , walstromite-structured CaSiO_3 , and titanite-structured CaSi_2O_5 were found as mineral inclusions in diamonds from the mantle [1,2]. While residing in the mantle, the continental crust material may interact with the surrounding MgO-rich mantle [3] and produce some special calcium magnesium silicates such as merwinite ($\text{Ca}_3\text{MgSi}_2\text{O}_8$), diopside ($\text{CaMgSi}_2\text{O}_6$), monticellite (CaMgSiO_4), and akermanite ($\text{Ca}_2\text{MgSi}_2\text{O}_7$). Among these calcium magnesium silicates, merwinite has been discovered as mineral inclusions in some diamonds from São Luiz, Brazil [4], suggesting that the interaction between the subducted CaO- and SiO_2 -rich continental crust material and the MgO-rich mantle material happens indeed.

Bredigite, with a typical composition $\text{Ca}_7\text{MgSi}_4\text{O}_{16}$, is such a potential calcium magnesium orthosilicate, which may form by the interaction between the subducted Ca-rich continental material and the MgO-rich mantle material at appropriate P - T conditions. The word “bredigite”, abbreviated as Bre hereafter, was first used by Tilley and Vincent [5] to describe a mineral coexisting with spurrite, larnite, and gehlenite in the contact zone of Chalk and Tertiary dolerite at Scawt Hill, Northern Ireland. It caused substantial confusion

in terms of chemical composition, phase stability, and crystallographic structure [5–19]. Thanks to enormous effort along all these years, it has become generally clear that the Bre from Scawt Hill is compositionally identical to "Phase T" experimentally observed by Gutt [7,8], with mutual substitution of Ca and Mg to some small extents [17,20] but without any significant Ba in the structure [11,14,16,19]. It has also become clear that Bre is stable up to ~1372 °C at ambient P [8–10,12,17]. Recently Xiong [20] experimentally demonstrated that Bre is stable at ~1.2 GPa.

The structure of Bre, however, remains unclear. A large number of studies provided powder X-ray diffraction patterns, but none generated single-crystal X-ray diffraction data [7,10,17,19]. It was proposed by Tilley and Vincent [5] that Bre might be structurally identical to a synthetic Ba-bearing calcium magnesium orthosilicate phase observed in some spiegeleisen slags, on the basis of the similarities of their morphologies and optical properties (compositionally approximating $\text{Ca}_{6.36}\text{Ba}_{0.32}\text{Mg}_{1.24}\text{Mn}_{0.36}\text{Si}_4\text{O}_{16}$). Accordingly, two single-crystal X-ray diffraction investigations were conducted with some crystals extracted from the spiegeleisen slags [6,13]. However, the synthetic crystals used in these studies contained a trigonal phase with a volume fraction up to ~20%, which substantially reduced the quality of the X-ray data. Additionally, it was rather unclear how the incorporation of Ba into the crystals might have distorted the structure, as Ba is significantly larger than Ca (e.g., the cation radius of 12-fold Ba is 1.61 Å whereas that of 12-fold Ca is 1.34 Å [21]). Indeed, Moseley and Glasser proposed different structures for them, with the Ba-bearing phase crystallizing in the space group $Pmn2$ and the Ba-free phase in the space group $Pmnn$ [17].

Along with the geological significance of Bre, Bre is not only an excellent bioactive ceramic [22] but also a high-quality phosphor candidate emitting special lights when doped with some particular rare earth elements [23]. A good understanding of the detailed structure of Bre will certainly benefit all these research fields.

Here, we synthesized the $\text{Ca}_7\text{MgSi}_4\text{O}_{16}$ -Bre by a solid-state method at high-temperature and high-pressure conditions, and determined its structure using single-crystal X-ray diffraction method. In addition, we theoretically calculated some of its thermodynamic properties using first-principles simulations. Before this study, there were no thermodynamic data for the $\text{Ca}_7\text{MgSi}_4\text{O}_{16}$ -Bre [24].

2. Experimental and Theoretical Methods

2.1. Synthesis

The $\text{Ca}_7\text{MgSi}_4\text{O}_{16}$ -Bre investigated in this study was synthesized by a solid-state reaction method at high P - T conditions. The starting material was made as follows: (1) 99.9% pure chemical powders CaCO_3 , MgO , and SiO_2 from Alfa Aesar (Alfa Aesar, Haverhill, MA, USA) were pretreated at 1 atm and 723 K for 72 hours to remove any absorbed moisture, immediately weighed in a mole ratio of 7:1:4, and then ground and homogenized in an agate mortar; (2) the resulting mixture was pressed into a pellet and degassed in a Pt crucible at 1 atm and 1273 K for 48 hours; (3) the degassed pellet was crushed and ground into a fine powder, which was further stored in a drying oven at 383 K and used as the starting material for a later synthesizing experiment. The starting material was loaded in a Pt capsule (10 mm in length and 2.5 mm in diameter) with both ends sealed using an arc-welding technique. The synthesizing experiment was carried out with a non-end loaded piston-cylinder apparatus installed at the High-Pressure Laboratory of Peking University (Quickpress 3.0, Depths of The Earth Company, Cave Creek, AZ, USA) [25]. The experimental assembly and high- P experimental technique were generally identical to those reported in Liu and Fleet [26]. The experimental P - T conditions were 1.2 GPa and 1373 K, and the heating time was 7 days.

2.2. Characterization

The high- P experimental product was polished with a series of diamond pastes, cleaned in alcohol using an ultrasonic washing machine, carbon-coated, and then exam-

ined for texture and composition respectively with a scanning electron microscope (Quanta 650 FEG, FEI Company, Hillsboro, OR, USA) and an electron microprobe (JXA-8100, JEOL, Tokyo, Japan). It was found out that the product contained a single crystalline phase with grain sizes ranging from 50–100 microns (Supplementary Materials Figure S1). Moreover, 13 electron microprobe analyses performed on randomly selected grains suggested the following chemical formula $\text{Ca}_{7.01(2)}\text{Mg}_{1.01(1)}\text{Si}_{3.99(1)}\text{O}_{16}$, closely matching the targeted formula $\text{Ca}_7\text{MgSi}_4\text{O}_{16}$. The product was eventually slightly pulverized, and some loose grains with appropriate sizes and shapes were hand-picked for a later single-crystal X-ray diffraction experiment. The rest of the sample was ground down to a fine powder and analyzed with a powder X-ray diffractometer (D/Max 2550 V/PC with graphite-monochromated Cu $K\alpha$ radiation, Rigaku Corporation, Tokyo, Japan) at ambient P – T conditions. The powder XRD pattern of the $\text{Ca}_7\text{MgSi}_4\text{O}_{16}$ -Bre, as shown in Figure 1, is consistent with the simulated XRD pattern based on the single-crystal structural analysis (more later), indicating that they are isostructural.

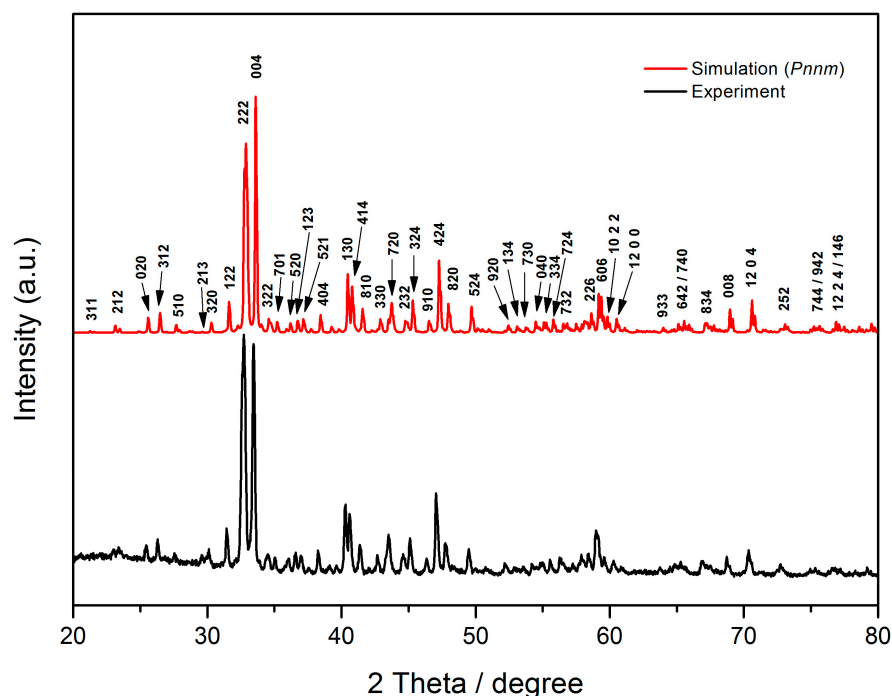


Figure 1. Experimental and simulated powder X-ray diffraction patterns of $\text{Ca}_7\text{MgSi}_4\text{O}_{16}$ -Bre (bredigite). Numbers represent the hkl indexes.

2.3. Single-Crystal X-Ray Diffraction

The single crystals were immersed in oil and examined under an optical microscope. A suitable crystal was then selected for the single-crystal X-ray diffraction analysis. The intensity data were collected on a Bruker Smart Apex III micro-focused diffractometer using Mo $K\alpha$ radiation ($\lambda = 0.71073$ nm). The raw data were processed and corrected for the absorption effects using the programs SAINT+ and SADAB. An initial structure solution was obtained via direct methods and refined by a full-matrix least-squares method using the SHELXT software included in the SHELXTL package. All heaviest atoms were first located unambiguously in the Fourier maps, and the O atoms were later found in the subsequent difference Fourier maps. All atoms were refined with the anisotropic displacement parameters. For the atoms with $I > 2\sigma(I)$, their atomic coordinates and anisotropic thermal parameters were included in the final cycles of the least-squares refinement.

2.4. Computational Method

The first-principles simulations carried out to investigate the compressibility of the $\text{Ca}_7\text{MgSi}_4\text{O}_{16}$ -Bre were deployed with the CASTEP code using density functional theory [27,28] and planewave pseudopotential technique [29]. The exchange–correlation interaction was treated by the generalized gradient approximation (GGA) with the Perdew–Burke–Ernzerhof (PBE) functional [30], and a convergence criterion of 5×10^{-7} eV/atom was used in the self-consistent field calculations. We employed a planewave basis set with a cutoff of 990 eV to expand the electronic wave functions, and a norm-conserving pseudopotential to model the ion–electron interaction [31,32]. We sampled the irreducible Brillouin zone with a $2 \times 6 \times 4$ Monkhorst-Pack grid [33]. The effects of using larger cutoff and k point mesh on the calculated properties were found to be insignificant. The computation cell contained four $\text{Ca}_7\text{MgSi}_4\text{O}_{16}$ -Bre molecules (in total 112 atoms), with the initial structure model from our single-crystal X-ray analysis. The equilibrium lattice parameters and internal coordinates at different pressures were optimized by minimizing the Hellmann–Feynman force on the atoms and simultaneously achieving the desired hydrostatic stress tensor. These theoretical techniques were used in our previous studies for the structures and thermodynamics of some silicate minerals [34,35].

Based on the optimized structure, the phonon dispersions and vibrational density of the states (VDoS) of the $\text{Ca}_7\text{MgSi}_4\text{O}_{16}$ -Bre were further calculated by diagonalizing the dynamical matrix with density functional perturbation theory [36,37]. The q-vector grid spacing for interpolation was 0.05 \AA^{-1} , which represented the average distance between the Monkhorst-Pack q-points used in the dynamical matrix calculations. The phonon dispersions were obtained at the high-symmetry points (G, Z, T, Y, S, X, U, R). The coordinates of these points on the surface of the Brillouin zone were $G = (0 \ 0 \ 0)$, $Z = (0 \ 0 \ 1/2)$, $T = (-1/2 \ 0 \ 1/2)$, $Y = (-1/2 \ 0 \ 0)$, $S = (-1/2 \ 1/2 \ 0)$, $X = (0 \ 1/2 \ 0)$, $U = (0 \ 1/2 \ 1/2)$, $R = (-1/2 \ 1/2 \ 1/2)$.

3. Results and Discussions

3.1. Structural Analysis

Moore and Araki [13] collected single-crystal X-ray diffraction data from the Ba-rich, Bre-like phase ($\text{Ca}_{6.15}\text{Ba}_{0.3}\text{Mg}_{1.2}\text{Mn}_{0.35}\text{Si}_4\text{O}_{16}$) extracted from the spiegeleisen slags and found its space group to be $Pnn2$. Taking into account the crystal chemistry of this phase, they performed a genealogy analysis of some phases in the CaO – MgO – SiO_2 system and proposed that the ideal Bre with the $\text{Ca}_7\text{MgSi}_4\text{O}_{16}$ composition might adopt the space group $Pnmm$.

Using our single-crystal X-ray diffraction data, we solved the structure in the space group $Pnmm$, with $a = 18.3434(17) \text{ \AA}$, $b = 6.7313(8) \text{ \AA}$, $c = 10.8844(12) \text{ \AA}$, $\alpha = 90^\circ$, $\beta = 90^\circ$, $\gamma = 90^\circ$, and $V = 1344.0(3) \text{ \AA}^3$ (Table 1). In this structure, each asymmetric unit contains two distinct Mg sites, three distinct Si sites, and six distinct Ca sites (for their coordinates and equivalent isotropic displacement parameters, see Table 2). As shown in Figure 2a, both Mg atoms are coordinated to six bridging O atoms to form $[\text{MgO}_6]$ octahedra. The Mg1–O bond lengths vary from 2.003(4) to 2.163(4) \AA , the Mg2–O bond lengths from 2.044(4) to 2.080(6) \AA , and the O–Mg–O angles from $87.33(15)^\circ$ to $180.000(1)^\circ$ (Table 3). All the Si sites are in 4-fold coordination, with the Si–O bond lengths varying from 1.594(4) to 1.637(4) \AA (Table 3). Further, every $[\text{SiO}_4]$ tetrahedron shares two O corners with two neighboring $[\text{MgO}_6]$ octahedra, leading to the formation of an $[\text{Mg}–\text{O}–\text{Si}]$ chain, which runs along the c -axis (Figure 2b). The $[\text{Mg}–\text{O}–\text{Si}]$ chains are the basic structural units of the $\text{Ca}_7\text{MgSi}_4\text{O}_{16}$ -Bre. The Ca sites are much more complicated (Table 3): Ca1, 6-coordinate (Ca1–O ranging from 2.275(5) to 2.465(4) \AA); Ca2, 10-coordinate (Ca2–O ranging from 2.305(5) to 2.886(4) \AA); Ca3, 7-coordinate (Ca3–O ranging from 2.212(6) to 2.989(4) \AA); Ca4, 7-coordinate (Ca4–O ranging from 2.327(6) to 2.579(5) \AA); Ca5, 9-coordinate (Ca5–O, ranging from 2.253(4) to 2.938(5) \AA); Ca6, 8-coordinate (Ca6–O ranging from 2.308(4) to 2.701(4) \AA).

Table 1. Crystal data for bredigite structure and bredigite-like structure.

Empirical Formula	Ca ₇ MgSi ₄ O ₁₆ ^a	Ca ₁₄ Mg ₂ Si ₈ O ₃₂ ^b	Ca _{6.15} Ba _{0.3} Mg _{1.2} Mn _{0.35} Si ₄ O ₁₆ ^c
Crystal system	Orthorhombic	Orthorhombic	Orthorhombic
Space group	<i>Pnmm</i>	<i>Pnn2</i>	<i>Pnn2</i>
Unit cell dimensions (Å)	a = 18.3434(17) b = 6.7313(8) c = 10.8844(12)	a' = 18.343(4) b' = 6.7313(13) c' = 10.884(2)	10.909(9) 18.34(1) 6.739(9)
Volume (Å ³)	1344.0(3)	1344.0(5)	1348(4)
Z	4	2	/
Crystal size (mm ³)	0.06 × 0.05 × 0.05	0.06 × 0.05 × 0.05	/
Theta range for data collection (°)	2.18 to 28.37	2.18 to 28.37	/
Limiting indices	−24 ≤ h ≤ 24 −9 ≤ k ≤ 5 −13 ≤ l ≤ 14	−24 ≤ h ≤ 24 −9 ≤ k ≤ 5 −13 ≤ l ≤ 14	/
Independent reflections	1756 [R(int) = 0.0483]	3101 [R(int) = 0.0444]	/
Completeness	99.50%	99.50%	/
Refinement method	Full-matrix least-squares on F ²	Full-matrix least-squares on F ²	/
Data/restraints/parameters	1756/0/147	3101/1/255	/
Goodness-of-fit on F ²	1.003	1.064	/
Final R indices [I > 2σ(I)]	R ₁ = 0.0472, wR ₂ = 0.1132	R ₁ = 0.0486, wR ₂ = 0.1095	/
R indices (all data)	R ₁ = 0.0675, wR ₂ = 0.1259	R ₁ = 0.0753, wR ₂ = 0.1279	/
Largest diff. peak and hole (e Å ^{−3})	0.877 and −0.720	0.758 and −0.752	/

^a Data refined in space group *Pnmm*. ^b Data refined in space group *Pnn2*. ^c Moore and Araki [13], original formula Ca_{24.6}Ba_{1.2}Mg_{4.8}Mn_{1.4}[SiO₄]₁₆.

Table 2. Atomic coordinates (x, y, z) and equivalent isotropic displacement parameters (U(eq)) for Ca₇MgSi₄O₁₆-Bre (*Pnmm*).

Atom Label	x	y	z	U(eq)
Ca(1)	0.5000	0.5000	1.0000	18(1)
Ca(2)	0.5000	0.5000	0.5000	41(1)
Ca(3)	0.3328(1)	0.8028(2)	1.0000	15(1)
Ca(4)	0.6733(1)	0.1718(2)	0.5000	14(1)
Ca(5)	0.4119(1)	0.1582(2)	0.7486(1)	15(1)
Ca(6)	0.7726(1)	0.9989(2)	0.2316(1)	10(1)
Mg(1)	0.5000	1.0000	1.0000	9(1)
Mg(2)	0.5000	1.0000	0.5000	8(1)
O(1)	0.2887(2)	0.2570(6)	1.1220(4)	14(1)
O(2)	0.6968(2)	0.8473(6)	0.3803(4)	16(1)
O(3)	0.4757(2)	0.7809(6)	0.8606(4)	16(1)
O(4)	0.3389(2)	0.8100(6)	0.7862(4)	13(1)
O(5)	0.3760(3)	0.4959(8)	1.0000	14(1)
O(6)	0.4115(2)	0.4895(6)	0.7191(4)	19(1)
O(7)	0.3978(3)	0.1045(8)	1.0000	18(1)
O(8)	0.5764(3)	0.7718(8)	0.5000	15(1)
O(9)	0.6946(3)	0.5126(8)	0.5000	18(1)
O(10)	0.4444(2)	0.8409(7)	0.6295(4)	25(1)
Si(1)	0.3382(1)	0.2828(3)	1.0000	8(1)
Si(2)	0.6638(1)	0.7355(3)	0.5000	9(1)
Si(3)	0.4192(1)	0.7194(2)	0.7518(1)	9(1)

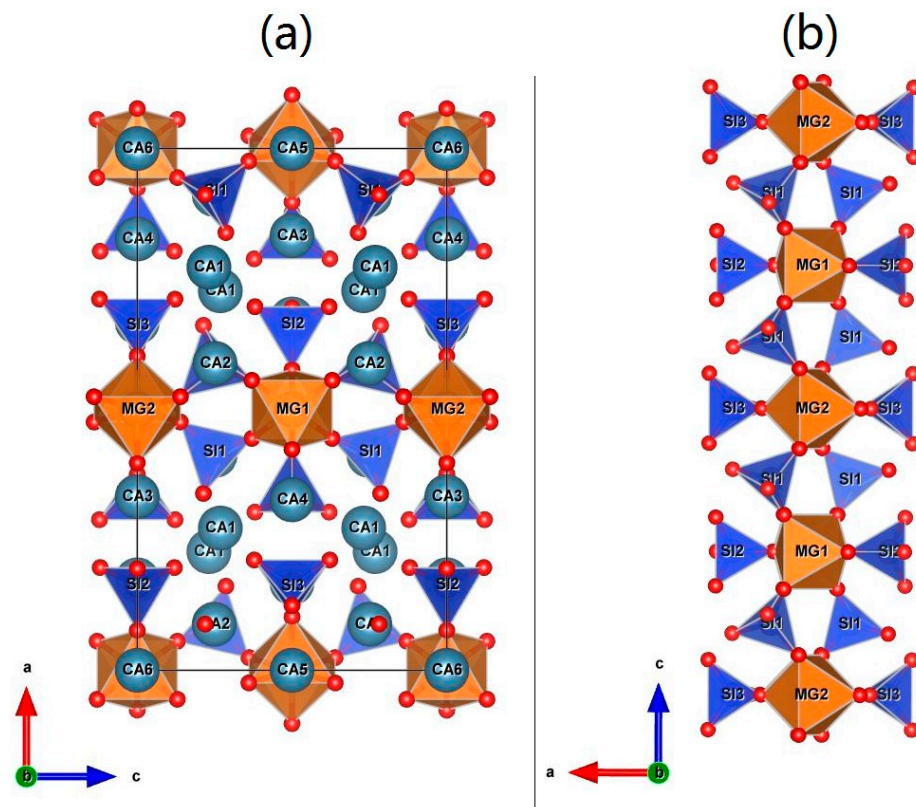


Figure 2. Polyhedral views of (a) $\text{Ca}_7\text{MgSi}_4\text{O}_{16}$ -Bre structure in space group $Pnmm$ and (b) $[\text{Mg}-\text{O}-\text{Si}]$ chains.

Table 3. Selected bond lengths (Å) and angles ($^\circ$) for $\text{Ca}_7\text{MgSi}_4\text{O}_{16}$ ($Pnmm$).

Bond ^a	Bond Length	Bond ^a	Bond Angle
Ca(1)–O(5)	2.275(5)	O(7)#7–Mg(1)–O(7)#1	180.000(1)
Ca(1)–O(5)#1	2.275(5)	O(7)#7–Mg(1)–O(3)	92.67(15)
Ca(1)–O(3)#2	2.465(4)	O(7)#1–Mg(1)–O(3)	87.33(15)
Ca(1)–O(3)#3	2.465(4)	O(7)#7–Mg(1)–O(3)#18	87.33(15)
Ca(1)–O(3)#1	2.465(4)	O(7)#1–Mg(1)–O(3)#18	92.67(15)
Ca(1)–O(3)	2.465(4)	O(3)–Mg(1)–O(3)#18	180.000(1)
Ca(2)–O(8)#5	2.305(5)	O(7)#7–Mg(1)–O(3)#3	92.67(15)
Ca(2)–O(8)	2.305(5)	O(7)#1–Mg(1)–O(3)#3	87.33(15)
Ca(2)–O(10)	2.880(4)	O(3)–Mg(1)–O(3)#3	89.1(2)
Ca(2)–O(10)#6	2.880(4)	O(3)#18–Mg(1)–O(3)#3	90.9(2)
Ca(2)–O(10)#5	2.880(4)	O(7)#7–Mg(1)–O(3)#19	87.33(15)
Ca(2)–O(10)#2	2.880(4)	O(7)#1–Mg(1)–O(3)#19	92.67(15)
Ca(2)–O(6)#6	2.886(4)	O(3)–Mg(1)–O(3)#19	90.9(2)
Ca(2)–O(6)#2	2.886(4)	O(3)#18–Mg(1)–O(3)#19	89.1(2)
Ca(2)–O(6)	2.886(4)	O(3)#3–Mg(1)–O(3)#19	180.000(1)
Ca(2)–O(6)#5	2.886(4)	O(10)#6–Mg(2)–O(10)#19	180.0(2)
Ca(3)–O(5)	2.212(6)	O(10)#6–Mg(2)–O(10)	87.3(3)
Ca(3)–O(4)	2.330(4)	O(10)#19–Mg(2)–O(10)	92.7(3)
Ca(3)–O(4)#3	2.330(4)	O(10)#6–Mg(2)–O(10)#15	92.7(3)
Ca(3)–O(7)#7	2.355(6)	O(10)#19–Mg(2)–O(10)#15	87.3(3)
Ca(3)–O(9)#8	2.823(6)	O(10)–Mg(2)–O(10)#15	180
Ca(3)–O(2)#8	2.989(4)	O(10)#6–Mg(2)–O(8)	87.11(16)
Ca(3)–O(2)#9	2.989(4)	O(10)#19–Mg(2)–O(8)	92.89(16)
Ca(4)–O(9)	2.327(6)	O(10)–Mg(2)–O(8)	87.11(16)
Ca(4)–O(1)#10	2.544(4)	O(10)#15–Mg(2)–O(8)	92.89(16)
Ca(4)–O(1)#11	2.544(4)	O(10)#6–Mg(2)–O(8)#15	92.89(16)
Ca(4)–O(2)#4	2.580(4)	O(10)#19–Mg(2)–O(8)#15	87.11(16)

Table 3. Cont.

Bond ^a	Bond Length	Bond ^a	Bond Angle
Ca(4)–O(2)#12	2.580(4)	O(10)–Mg(2)–O(8)#15	92.89(16)
Ca(4)–O(10)#5	2.579(5)	O(10)#15–Mg(2)–O(8)#15	87.11(16)
Ca(4)–O(10)#2	2.579(5)	O(8)–Mg(2)–O(8)#15	180.000(1)
Ca(5)–O(6)	2.253(4)	O(5)–Si(1)–O(1)#3	109.92(18)
Ca(5)–O(3)#2	2.430(4)	O(5)–Si(1)–O(1)	109.92(18)
Ca(5)–O(2)#5	2.439(4)	O(1)#3–Si(1)–O(1)	110.3(3)
Ca(5)–O(10)#4	2.568(5)	O(5)–Si(1)–O(7)	111.9(3)
Ca(5)–O(4)#4	2.730(4)	O(1)#3–Si(1)–O(7)	107.37(19)
Ca(5)–O(1)#3	2.745(4)	O(1)–Si(1)–O(7)	107.37(19)
Ca(5)–O(8)#5	2.7554(16)	O(9)–Si(2)–O(8)	119.3(3)
Ca(5)–O(7)	2.7718(15)	O(9)–Si(2)–O(2)#6	107.6(2)
Ca(5)–O(10)#2	2.938(5)	O(8)–Si(2)–O(2)#6	107.40(19)
Ca(6)–O(1)#13	2.308(4)	O(9)–Si(2)–O(2)	107.6(2)
Ca(6)–O(2)	2.365(4)	O(8)–Si(2)–O(2)	107.40(19)
Ca(6)–O(1)#14	2.377(4)	O(2)#6–Si(2)–O(2)	106.9(3)
Ca(6)–O(4)#15	2.424(4)		
Ca(6)–O(4)#16	2.482(4)		
Ca(6)–O(6)#16	2.553(4)		
Ca(6)–O(9)#17	2.5931(17)		
Ca(6)–O(2)#17	2.701(4)		
Mg(1)–O(7)#7	2.003(5)		
Mg(1)–O(7)#1	2.003(5)		
Mg(1)–O(3)	2.163(4)		
Mg(1)–O(3)#18	2.163(4)		
Mg(1)–O(3)#3	2.163(4)		
Mg(1)–O(3)#19	2.163(4)		
Mg(2)–O(10)#6	2.044(4)		
Mg(2)–O(10)#19	2.044(4)		
Mg(2)–O(10)	2.044(4)		
Mg(2)–O(10)#15	2.044(4)		
Mg(2)–O(8)	2.080(6)		
Mg(2)–O(8)#15	2.080(6)		
Si(1)–O(5)	1.594(6)		
Si(1)–O(1)#3	1.619(4)		
Si(1)–O(1)	1.619(4)		
Si(1)–O(7)	1.623(6)		
Si(2)–O(9)	1.603(6)		
Si(2)–O(8)	1.622(6)		
Si(2)–O(2)#6	1.622(4)		
Si(2)–O(2)	1.622(4)		
Si(3)–O(3)	1.627(4)		
Si(3)–O(4)	1.637(4)		
Si(3)–O(6)	1.594(4)		
Si(3)–O(10)	1.629(4)		

^a Symmetry transformations used to generate equivalent atoms: #1 $-x + 1, -y + 1, -z + 2$; #2 $-x + 1, -y + 1, z$; #3 $x, y, -z + 2$; #4 $x, y - 1, z$; #5 $-x + 1, -y + 1, -z + 1$; #6 $x, y, -z + 1$; #7 $x, y + 1, z$; #8 $x - 1/2, -y + 3/2, z + 1/2$; #9 $x - 1/2, -y + 3/2, -z + 3/2$; #10 $x + 1/2, -y + 1/2, z - 1/2$; #11 $x + 1/2, -y + 1/2, -z + 3/2$; #12 $x, y - 1, -z + 1$; #13 $x + 1/2, -y + 3/2, -z + 3/2$; #14 $-x + 1, -y + 1, z - 1$; #15 $-x + 1, -y + 2, -z + 1$; #16 $x + 1/2, -y + 3/2, z - 1/2$; #17 $-x + 3/2, y + 1/2, -z + 1/2$; #18 $-x + 1, -y + 2, -z + 2$; #19 $-x + 1, -y + 2, z$.

We also attempted to solve the structure in the space group $Pnn2$, with the unit-cell parameters a', b' , and c' , respectively, equivalent to the unit-cell parameters a, b , and c of the $Pnmm$ space group (Table 1). The resulting atomic coordinates and equivalent isotropic displacement parameters are listed in Supplementary Table S1. In the $Pnn2$ model, the atoms Ca1, Ca2, Mg1, and Mg2 deviate from symmetric centers in the $Pnmm$ model (Figure 3), which splits the mirror plane and lowers the symmetry from $Pnmm$ to $Pnn2$. Nevertheless, the atom arrangement in the $Pnn2$ model is very similar to that in the $Pnmm$

model. We therefore used the PLATON software to exam the relations between these two structural models. The result suggests that the $Pnn2$ model can transform to the $Pnmm$ model via the following matrix operation:

$$\begin{pmatrix} x' & y' & z' \end{pmatrix} = \begin{pmatrix} x & y & z \end{pmatrix} \times \begin{bmatrix} -1.0000 & 0.0000 & 0.0000 \\ 0.0000 & -1.0000 & 0.0000 \\ 0.0000 & 0.0000 & 1.0000 \end{bmatrix} + \begin{pmatrix} 0.0000 & 0.0000 & 0.2344 \end{pmatrix} \quad (1)$$

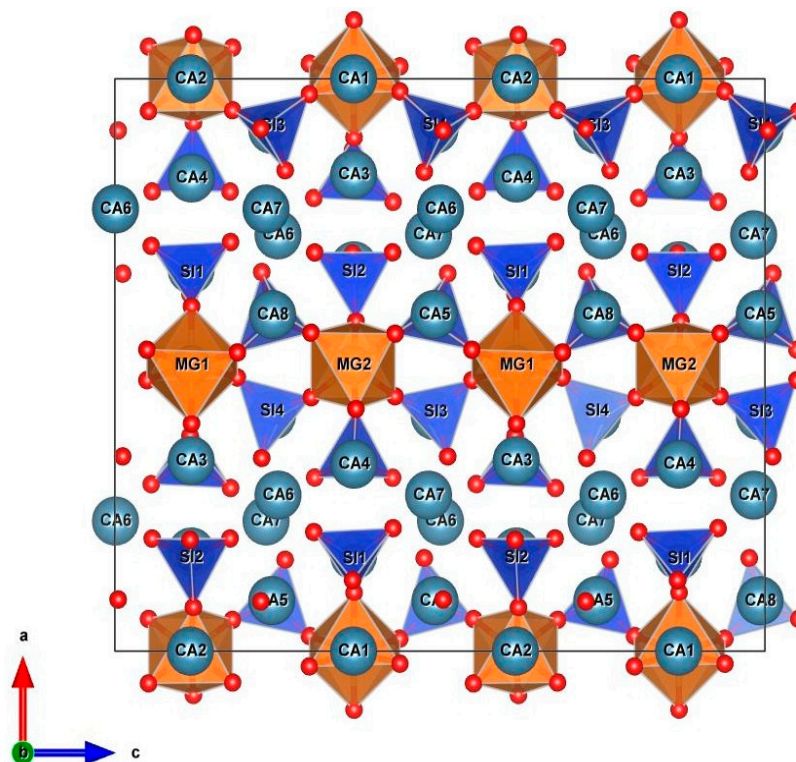


Figure 3. Polyhedral view of Bre structure in space group $Pnn2$.

The average deviation of the atom positions in the two $Pnmm$ models is just 0.039 Å. This indicates that the space group of the $\text{Ca}_7\text{MgSi}_4\text{O}_{16}$ -Bre is $Pnmm$ indeed.

It is thus clear that due to substantial amounts of Ba^{2+} and Mn^{2+} substitutions, respectively, for Ca^{2+} and Mg^{2+} , the atoms on the Ca2, Mg1, and Mg2 sites of the $Pnmm$ model can significantly depart from high-symmetry sites, leading to the space group $Pnn2$, as observed by Moore and Araki [13]. Recently, a natural Mn-free Bre with the composition $\text{Ca}_{7.006}\text{Na}_{0.015}\text{Ba}_{0.014}\text{Mg}_{0.938}\text{Si}_{4.000}\text{P}_{0.014}\text{O}_{16}$ was reported from the Hatrurim Complex, Negev Desert, Israel [38], and its space group was determined as $Pnmm$ as well. This suggests that small amounts of impurities such as Na, Ba, and P incorporated into the structure do not alter the basic crystallographic features of the $\text{Ca}_7\text{MgSi}_4\text{O}_{16}$ -Bre. As a result, it is important to investigate the physical–chemical properties of $\text{Ca}_7\text{MgSi}_4\text{O}_{16}$ -Bre.

3.2. Isothermal Bulk Modulus, Heat Capacity, and Entropy

The unit-cell parameters of the $\text{Ca}_7\text{MgSi}_4\text{O}_{16}$ -Bre at zero pressure obtained from the first-principles calculation are summarized in Table 4. They compare well with the results obtained from the single-crystal X-ray diffraction data.

The E - V data from our static calculation for the $\text{Ca}_7\text{MgSi}_4\text{O}_{16}$ -Bre are shown in Figure 4. To determine the isothermal bulk modulus, the third-order E - V Birch–Murnaghan equation of state [39] was fitted with the E - V data by a least-squares method:

$$E(V) = E_0 + \frac{9B_0V_0}{16} \left[\left(\frac{V_0}{V} \right)^{\frac{2}{3}} - 1 \right]^2 \times \left[(B'_0 - 4) \times \left(\frac{V_0}{V} \right)^{\frac{2}{3}} - B'_0 + 6 \right] \quad (2)$$

where E is the free energy, B_0 is the isothermal bulk modulus, B'_0 is the first pressure derivative of B_0 , V_0 is the volume at zero pressure, and V are the volumes at other pressures. When B'_0 is set as 4, B_0 is 93.1(22) GPa and V_0 is 1394.2(16) Å³. If B'_0 is not fixed, B_0 is 90.6(4) GPa, B'_0 is 5.7(1), and V_0 is 1388.0(6) Å³.

Table 4. Comparison between energy-optimized (0 P and 0 K) and experimentally refined (1 atm and 298 K) unit-cell parameters of the Ca₇MgSi₄O₁₆-Bre (*Pnnm*).

Cell Parameters	Experimental	Calculated	R.D. (%) ^a
a	18.3434(17) Å	18.5125 Å	~0.92
b	6.7313(8) Å	6.7833 Å	~0.77
c	10.8844(12) Å	11.0067 Å	~1.12
V	1344.0(3) Å ³	1382.18 Å ³	~2.84

^a Relative difference.

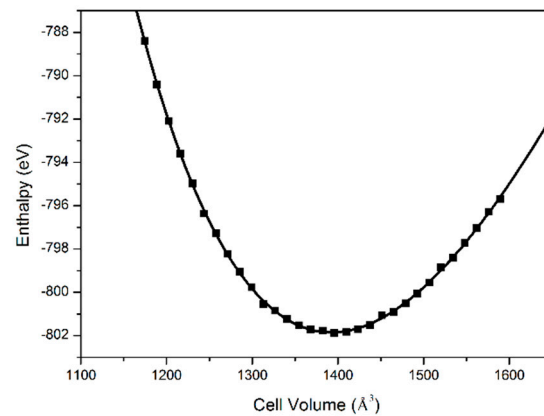


Figure 4. Total energy of Ca₇MgSi₄O₁₆-Bre as a function of cell volume (at 0 K). Symbols represent simulated results while curve stands for the fitted E - V third-order Birch–Murnaghan equation of state ($B_0 = 90.6(4)$ GPa, $B'_0 = 5.7(1)$, and $V_0 = 1388.0(6)$ Å³).

We calculated the phonon dispersions and VDoS. The dynamical matrices were computed at 21 wavevectors in the Brillouin zone of the cell and interpolated to obtain the bulk phonon dispersions. Figure 5 shows the dispersion curves along several symmetry directions and the VDoS. Clearly, the Ca₇MgSi₄O₁₆-Bre in the space group *Pnnm* is dynamically stable.

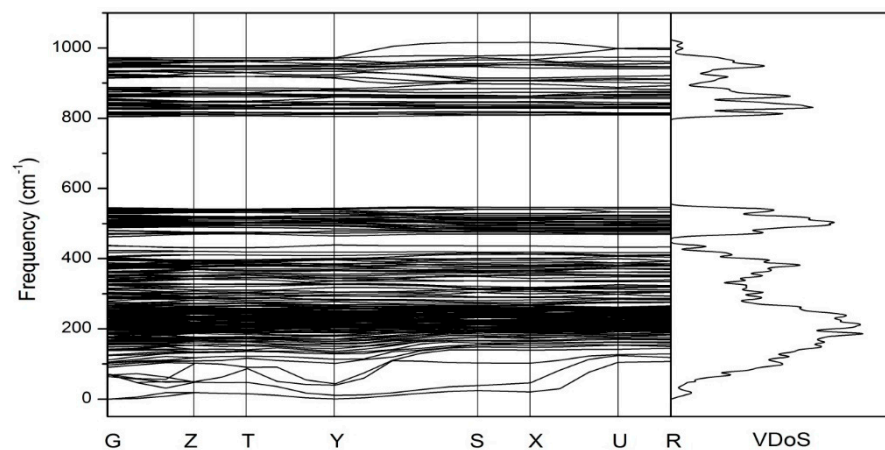


Figure 5. Phonon dispersions and vibrational density of the states (VDoS) of Ca₇MgSi₄O₁₆-Bre ($V = 1382.18$ Å³).

The phonon spectrum for the $\text{Ca}_7\text{MgSi}_4\text{O}_{16}$ -Bre has been used to compute the internal energy (E) and isochoric heat capacity (C_v) as functions of temperature. The temperature dependence of the E was obtained by the following equation,

$$E(T) = E_{tot} + E_{zp} + \int \frac{h\omega}{\exp\left(\frac{h\omega}{kT}\right) - 1} F(\omega) d\omega \quad (3)$$

with E_{tot} representing the total electronic energy at 0 K, E_{zp} the zero-point vibrational energy, h the Planck's constant, k the Boltzmann constant, and $F(\omega)$ the vibrational density of states. We evaluated the E_{zp} term in Equation (3) using the following equation,

$$E_{zp} = \int F(\omega) h\omega d\omega \quad (4)$$

Furthermore, we approximated the lattice contribution to C_v with the following equation:

$$C_v(T) = k \int \frac{\left(\frac{h\omega}{kT}\right)^2 \exp\left(\frac{h\omega}{kT}\right)}{\left[\left(\frac{h\omega}{kT}\right)^2 - 1\right]^2} F(\omega) d\omega \quad (5)$$

The C_v result calculated in this way is shown in Table 5.

C_p was calculated by adding an anharmonic effect to C_v obtained from the above calculations, using the following equation:

$$C_p = C_v + \alpha_T^2 B_T V_T T \quad (6)$$

where α_T , B_T , and V_T are the thermal expansion coefficient, isothermal bulk modulus, and volume at 1 atm and T (K), respectively. The thermal expansion coefficient, as shown in Figure 6 (with some values at some selected temperatures listed in Table 5), was calculated by the Gibbs software through a quasi-harmonic Debye model [40]. The temperature derivative of B_T was assumed as zero in our calculation. V_T at T K was calculated with the following equation:

$$V_T = V_{298} \exp\left(\int_{298}^T \alpha_T dT\right) \quad (7)$$

where $V_{298} = 809.1(2) \text{ cm}^3/\text{mol}$. The calculated C_p values are listed in Table 5, and compared to the C_v values in Figure 7. The C_p values are divided into three T ranges, 10–100, 100–298, and 298–1000 K, and empirically fitted to the equation from [24], with the coefficients summarized in Table 6.

Table 5. Thermal expansion coefficient ($\times 10^5 \text{ K}^{-1}$), and heat capacity ($\text{J mol}^{-1} \text{ K}^{-1}$) of $\text{Ca}_7\text{MgSi}_4\text{O}_{16}$ -Bre at selected T (K).

T (K)	C_V ($\text{J mol}^{-1} \text{ K}^{-1}$)	C_P ($\text{J mol}^{-1} \text{ K}^{-1}$)	α_T ($\times 10^5 \text{ K}^{-1}$)
50	77.36	78.74	0.1048
100	221.73	224.49	0.6847
150	331.46	335.61	1.4269
200	409.8	415.35	1.9949
250	467.65	474.6	2.3858
300	511.55	519.9	2.6588
350	545.31	555.07	2.8590
400	571.5	582.67	3.0141
450	592.01	604.6	3.1394
500	608.23	622.25	3.2483
550	621.19	636.64	3.3451
600	631.67	648.55	3.4340
650	640.22	658.55	3.5179

Table 5. Cont.

T (K)	C_V (J mol ⁻¹ K ⁻¹)	C_P (J mol ⁻¹ K ⁻¹)	α_T ($\times 10^5$ K ⁻¹)
700	647.27	667.05	3.5991
750	653.15	674.37	3.6775
800	658.08	680.76	3.7579
850	662.26	686.4	3.8385
900	665.82	691.44	3.9203
950	668.89	695.97	4.0040
1000	671.54	700.1	4.0903

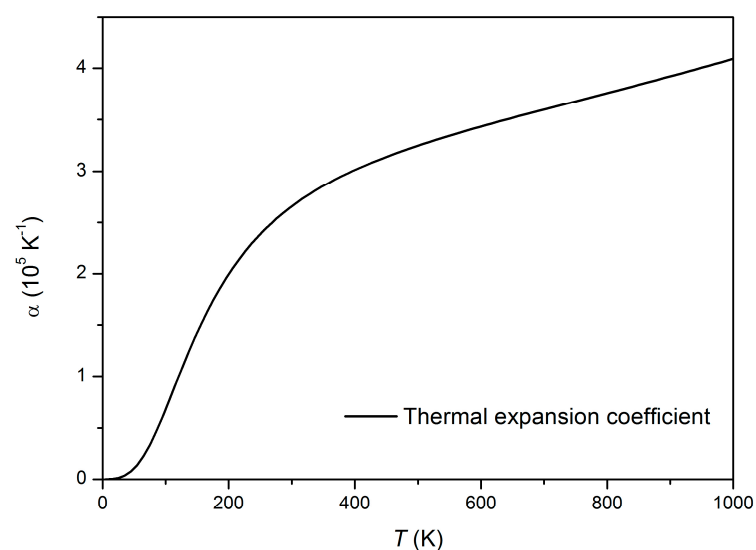


Figure 6. Calculated thermal expansion coefficient of Bre.

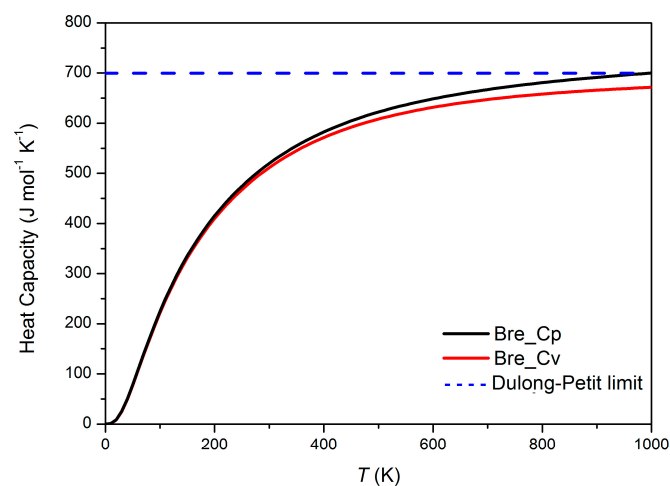


Figure 7. Isobaric and isochoric heat capacity (C_p and C_v , respectively) of $\text{Ca}_7\text{MgSi}_4\text{O}_{16}$ -Bre. Note that the C_v values remain lower than the harmonic limit of Dulong–Petit ($3R/M$, with R as the gas constant and M as the molar mass) for T less than 1000 K, suggesting that either the quantum effects for the ionic vibrations remain noticeable for this T range, or our C_v values have been slightly underestimated (presumably by a few percent) because the volume used in the calculation is for zero P and zero T .

Table 6. Coefficients of the C_p polynomials of $\text{Ca}_7\text{MgSi}_4\text{O}_{16}$ -Bre ($Pnmm$).

T Range: 10–100 K	T Range: 100–298 K	T Range: 298–1000 K
$k_0 = 2.8(6)$	$k_0 = -1.24(2) \times 10^2$	$k_0 = 8.22(2) \times 10^2$
$k_4 = -7.0(6) \times 10^{-1}$	$k_4 = 4.50(3)$	$k_1 = -3.76(6) \times 10^3$
$k_5 = 5.9(2) \times 10^{-2}$	$k_5 = -1.16(2) \times 10^{-2}$	$k_2 = -1.38(4) \times 10^7$
$k_6 = -3.0(1) \times 10^{-4}$	$k_6 = 1.23(3) \times 10^{-5}$	$k_3 = 1.61(8) \times 10^9$

$$^a C_p = k_0 + k_1 T^{-0.5} + k_2 T^{-2} + k_3 T^{-3} + k_4 T + k_5 T^2 + k_6 T^3 \text{ (J mol}^{-1} \text{ K}^{-1}\text{)}.$$

The C_p values have been applied to the calculation of the vibrational entropy at T K using the following equation,

$$S_T^0 = \int_0^T \frac{C_p}{T} dT \quad (8)$$

The vibrational entropy of the $\text{Ca}_7\text{MgSi}_4\text{O}_{16}$ -Bre at 298 K (S_{298}^0) is calculated as 534.1 (22) $\text{J mol}^{-1} \text{ K}^{-1}$.

4. Conclusions

$\text{Ca}_7\text{MgSi}_4\text{O}_{16}$ -Bre has been successfully synthesized at 1.2 GPa and 1373 K, and its structure has been determined by single-crystal X-ray diffraction data. We find that the $\text{Ca}_7\text{MgSi}_4\text{O}_{16}$ -Bre has the space group $Pnmm$. Although this space group may be reduced to the space group $Pnn2$ as significant amounts of Ba and Mn enter the structure, it tolerates low levels of chemical impurities such as Na, Ba, and P.

Some first-principles calculations have been carried out as well. The results suggest that the isothermal bulk modulus of the $\text{Ca}_7\text{MgSi}_4\text{O}_{16}$ -Bre is 90.6(4) GPa (with a pressure derivative of 5.7(1)), the isobaric heat capacity is $C_p = 8.22(2) \times 10^2 - 3.76(6) \times 10^3 T^{-0.5} - 1.384(4) \times 10^7 T^{-2} + 1.61(8) \times 10^9 T^{-3} \text{ J mol}^{-1} \text{ K}^{-1}$ (298–1000 K), and the standard vibrational entropy is $S_{298}^0 = 534.1$ (22) $\text{J mol}^{-1} \text{ K}^{-1}$.

Supplementary Materials: The followings are available online at <https://www.mdpi.com/2073-4352/11/1/14/s1>, Figure S1: Back scattered electron (BSE) image of bredigite, Table S1: atomic coordinates and $U(\text{eq})$ for $\text{Ca}_7\text{MgSi}_4\text{O}_{16}$ ($Pnn2$), crystal reflection data files (bredigite.HKL) and crystallographic information files (bredigite.CIF).

Author Contributions: X.B., synthesizing and characterizing the material, collecting and refining the single-crystal X-ray data, performing theoretical calculations, interpreting the results, and writing the paper; M.H., designing and supervising the project and discussing and interpreting the results; Z.Z., supervising theoretical calculation; X.L., designing and supervising the project, interpreting and finalizing the results, writing and finalizing the paper. All authors have read and agreed to the published version of the manuscript.

Funding: This study is financially supported by the Strategic Priority Research Programs (B) of the Chinese Academy of Sciences (grant no. XDB18000000 and XDB42000000) and by the Program of the National Mineral Rock and Fossil Specimens Resource Center from MOST, China.

Acknowledgments: We thank Hejin Wang for his help with the powder X-ray diffraction analysis, and Xiaoli Li for his help with the electron microprobe analyses.

Conflicts of Interest: The authors declare no conflict of interests.

References

- Joswig, W.; Stachel, T.; Harris, J.W.; Baur, W.H.; Brey, G.P. New Ca-silicate inclusions in diamond-stracers from the lower mantle. *Earth Planet. Sci. Lett.* **1999**, *173*, 1–6. [[CrossRef](#)]
- Brenker, F.E.; Vincze, I.; Vekemans, B.; Nasdala, L.; Stachel, T.; Vollmer, C.; Kersten, M.; Somogyi, A.; Adams, F.; Joswig, W.; et al. Detection of a Ca-rich lithology in the Earth's deep (>300 km) convecting mantle. *Earth Planet. Sci. Lett.* **2005**, *236*, 579–587. [[CrossRef](#)]
- Ringwood, A.E. *Composition and Petrology of the Earth's Mantle*; McGraw-Hill: Sydney, Australia, 1975; pp. 1–618. ISBN 978-0070529328.

4. Zedgenizov, D.A.; Shatskiy, A.; Ragozin, A.L.; Kagi, H.; Shatsky, V.S. Merwinite in diamond from Sao Luiz, Brazil: A new mineral of the Ca-rich mantle environment. *Am. Mineral.* **2014**, *99*, 547–550. [[CrossRef](#)]
5. Tilley, C.E.; Vincent, H.C.G. The occurrence of an orthorhombic high-temperature form of Ca_2SiO_4 (bredigite) in the contact-zone and as a constituent of slags. *Mineral. Mag.* **1948**, *28*, 255–271.
6. Douglas, A.M.B. X-ray investigation of bredigite. *Mineral. Mag.* **1952**, *29*, 875–884. [[CrossRef](#)]
7. Gutt, W. A new calcium magnesium silicate. *Nature* **1961**, *190*, 339–340. [[CrossRef](#)]
8. Gutt, W. The system dicalcium silicate-merwinite. *Nature* **1965**, *207*, 184–185. [[CrossRef](#)]
9. Schlaudt, C.M.; Roy, D.M. The join Ca_2SiO_4 - CaMgSiO_4 . *J. Am. Ceram. Soc.* **1966**, *49*, 430–432. [[CrossRef](#)]
10. Biggar, G.M. Phase relationships of bredigite ($\text{Ca}_5\text{MgSi}_3\text{O}_{12}$) and of the quaternary compound ($\text{Ca}_6\text{MgAl}_8\text{SiO}_{21}$) in the system $\text{CaO-MgO-Al}_2\text{O}_3\text{-SiO}_2$. *Cem. Concr. Res.* **1971**, *1*, 493–513. [[CrossRef](#)]
11. Midgley, H.G.; Bennett, M. A microprobe analysis of larnite and bredigite from Scawt Hill, Larne, Northern Ireland. *Cem. Concr. Res.* **1971**, *1*, 413–418. [[CrossRef](#)]
12. Lin, H.C.; Foster, W.R. Stability relations of bredigite (5CaO.MgO.3SiO_2). *J. Am. Ceram. Soc.* **1975**, *58*, 73. [[CrossRef](#)]
13. Moore, P.B.; Araki, T. The crystal structure of bredigite and the genealogy of some alkaline earth orthosilicates. *Am. Mineral.* **1976**, *61*, 74–87.
14. Sarkar, S.L.; Jeffery, J.W. Electron microprobe analysis of Scawt Hill bredigite-larnite rock. *J. Am. Ceram. Soc.* **1978**, *61*, 177–178. [[CrossRef](#)]
15. Essene, E. The stability of bredigite and other Ca-Mg silicates. *J. Am. Ceram. Soc.* **1979**, *63*, 464–466. [[CrossRef](#)]
16. Bridge, T.E. Progressive metamorphism of Permian siliceous limestone and dolomite—a complete sequence around a monzonite intrusion, Marble Canyon, Diablo Plateau, West Texas. In *Trans Pecos Region (West Texas)*; Dickerson, P.W., Hoffer, J.M., Callender, J.F., Eds.; New Mexico Geological Society: Socorro, NM, USA, 1980; pp. 225–229.
17. Moseley, D.; Glasser, F.P. Identity, composition and stability of bredigite and phase T. *Cem. Concr. Res.* **1981**, *11*, 559–565. [[CrossRef](#)]
18. Moseley, D.; Glasser, F.P. Properties and composition of bredigite-structured phases. *J. Mater. Sci.* **1982**, *17*, 2736–2740. [[CrossRef](#)]
19. Sabine, P.A.; Styles, M.T.; Young, B.R. The nature and paragenesis of natural bredigite and associated minerals from Carneal and Scawt Hill, Co. Antrim. *Mineral. Mag.* **1985**, *49*, 663–670. [[CrossRef](#)]
20. Xiong, Z. 2015. High Temperature and High Pressure Study about the Ca-rich Silicates in the System Ca_2SiO_4 - $\text{Ca}_3\text{MgSi}_2\text{O}_8$. Ph.D. Thesis, Peking University, Beijing, China.
21. Shannon, R.D. Revised effective ionic radii and systematic studies of interatomic distances in halides and chalcogenides. *Acta Crystallogr.* **1976**, *32*, 751–767. [[CrossRef](#)]
22. Wu, C.; Chang, J.; Wang, J.; Ni, S.; Zhai, W. Preparation and characteristics of a calcium magnesium silicate (bredigite) bioactive ceramic. *Biomaterials* **2005**, *26*, 2925–2931. [[CrossRef](#)]
23. Jia, Y.; Qiao, H.; Zheng, Y.; Guo, N.; You, H. Synthesis and photoluminescence properties of Ce^{3+} and Eu^{2+} -activated $\text{Ca}_7\text{Mg}(\text{SiO}_4)_4$ phosphors for solid state lighting. *Phys. Chem. Chem. Phys.* **2017**, *14*, 3537–3542. [[CrossRef](#)]
24. Holland, T.J.B.; Powell, R. An improved and extended internally consistent thermodynamic dataset for phases of petrological interest, involving a new equation of state for solids. *J. Metamorph. Geol.* **2011**, *29*, 333–383. [[CrossRef](#)]
25. He, Q.; Liu, X.; Li, B.; Deng, L.; Chen, Z.; Liu, X.; Wang, H. Expansivity and compressibility of strontium fluorapatite and barium fluorapatite determined by in situ X-ray diffraction at high-T/P conditions: Significance of the M-site cations. *Phys. Chem. Miner.* **2013**, *40*, 29–40. [[CrossRef](#)]
26. Liu, X.; Fleet, M.E. Phase relations of nahcolite and trona at moderate P-T conditions. *J. Miner. Petrol. Sci.* **2009**, *104*, 25–36. [[CrossRef](#)]
27. Hohenberg, P.; Kohn, W. Inhomogeneous Electron Gas. *Phys. Rev.* **1964**, *136*, 864–871. [[CrossRef](#)]
28. Kohn, W.; Sham, L.J. Self-Consistent Equations Including Exchange and Correlation Effects. *Phys. Rev.* **1965**, *140*, 1133–1138. [[CrossRef](#)]
29. Payne, M.C.; Teter, M.P.; Allan, D.C.; Arias, T.A.; Joannopoulos, J.D. Iterative minimization techniques for ab initio total-energy calculations: Molecular dynamics and conjugate gradients. *Rev. Mod. Phys.* **1992**, *64*, 1045–1097. [[CrossRef](#)]
30. Perdew, J.; Burke, K.; Ernzerhof, M. Generalized Gradient Approximation Made Simple. *Phys. Rev. Lett.* **1996**, *77*, 3865–3868. [[CrossRef](#)]
31. Lin, J.; Qteish, A.; Payne, M.; Heine, V. Optimized and transferable nonlocal separable ab initio pseudopotentials. *Phys. Rev. B* **1993**, *47*, 4147–4180. [[CrossRef](#)]
32. Lee, M. Advanced Pseudopotentials for large scale electronic structure calculations. Ph.D. Dissertation, University of Cambridge, Cambridge, UK, 1995.
33. Monkhorst, H.; Pack, J. Special points for Brillouin-zone integrations. *Phys. Rev. B* **1976**, *13*, 5188–5192. [[CrossRef](#)]
34. Chang, L.; Liu, X.; Liu, H.; Kojitani, H.; Wang, S. Vibrational mode analysis and heat capacity calculation of $\text{K}_2\text{SiSi}_3\text{O}_9$ -wadeite. *Phys. Chem. Miner.* **2013**, *40*, 563–574. [[CrossRef](#)]
35. Xiong, Z.; Liu, X.; Shieh, S.R.; Wang, S.; Chang, L.; Tang, J.; Hong, X.; Zhang, Z.; Wang, H. Some thermodynamic properties of larnite ($\beta\text{-Ca}_2\text{SiO}_4$) constrained by high T/P experiment and/or theoretical simulation. *Am. Mineral.* **2016**, *101*, 277–288. [[CrossRef](#)]

36. Baroni, S.; Gironcoli, S.; Dal Corso, A.; Giannozzi, P. Phonons and related crystal properties from density-functional perturbation theory. *Rev. Mod. Phys.* **2001**, *73*, 515–562. [[CrossRef](#)]
37. Refson, K.; Tulip, P.; Clark, S. Variational density-functional perturbation theory for dielectrics and lattice dynamics. *Phys. Rev. B* **2006**, *73*, 155114–1551125. [[CrossRef](#)]
38. Kathlenberg, V.; Galuskina, I.; Krüger, B.; Pauluhn, A.; Galuskin, E. Structural investigations on bredigite from the Hatrurim Complex. *Miner. Petrol.* **2019**, *113*, 261–272. [[CrossRef](#)]
39. Birch, F. Finite Elastic Strain of Cubic Crystals. *Phys. Rev.* **1947**, *71*, 809–824. [[CrossRef](#)]
40. Blanco, M.A.; Francisco, E.; Luaña, V. GIBBS: Isothermal-isobaric thermodynamics of solids from energy curves using a quasi-harmonic Debye model. *Comput. Phys. Commun.* **2004**, *158*, 57–72. [[CrossRef](#)]